Proceedings of the 16th European Turbomachinery Conference (ETC16)
Turbomachinery, Fluid Dynamics and Thermodynamics,
March 24-28, 2025; Hannover, Germany

Aerodynamic scaling of a high-speed low-pressure turbine cascade, optimized for boundary layer similarity in a low-speed test rig

Giacomo Pastorino*[1,2], Elissavet Boufidi[1], Koen Hillewaert[2], and Fabrizio Fontaneto[1]

[1]Turbomachinery and Propulsion Department, von Karman Institute for Fluid Dynamics, Sint-Genesius-Rode, Belgium
[2]Faculté des Sciences appliquées, Université de Liège, Liège, Belgium

Abstract

Although high-speed testing closely reproduces real engine aerodynamics, low-speed experiments offer improved spatial and temporal measurement resolution, at lower operational costs. Nevertheless, the direct adoption of high-speed designs in low-speed facilities comes at the expense of a loss of representativity: the lower Mach number yields different loading distributions, hence non-similar boundary layers and performance. As a matter of fact, a geometry re-design is required that allows to respect the boundary layer driving parameters also when the kinematic similarity is not respected. This paper presents the procedure adopted to scale the SPLEEN C1 low-pressure turbine blade for low-speed testing. The pressure coefficient distribution of the high-speed blade was identified as the target scaling object to ensure that the boundary layers evolve under engine-representative pressure gradients. A preliminary sensitivity study, based on the Zweifel loading coefficient, revealed the need to modify both the pitch-to-chord ratio and the outlet flow angle to match the high-speed loading. The blade geometry was parametrized and iteratively modified in an optimization process coupled with the MISES cascade solver. The similarity between the boundary layers of the scaled and the high-speed blades is evaluated in terms of displacement thickness, momentum loss thickness, and skin friction coefficient. Additionally, the effects of low-speed scaling on profile losses and secondary flows are examined.

Keywords: Blade scaling, boundary layer scaling, low-speed flow, linear cascade, low-pressure turbine

1 Introduction

The development of innovative propulsive technologies continues to face significant challenges, particularly in the understanding and modeling of key physical phenomena. The design of modern ultra-high bypass ratio turbofans still strongly relies on low-fidelity simulations and low-order models, as high-fidelity alternatives would demand too many computational resources to be practical for preliminary design purposes [1]. Results from RANS solvers are often highly sensitive to the turbulence and transition models adopted, and still struggle to capture the boundary layer flow physics [2–4]. This is especially problematic for low-pressure turbines (LPTs) design, where the low Reynolds number at cruise conditions [5] can cause a separation bubble to form on the rear of the blade suction side. In LPTs, the profile loss – the biggest contributor to the overall loss budget [6] – strongly depends on both the presence of the separation bubble and the boundary layer transition location. Therefore, the current shortcomings in the prediction of boundary layers state affect the precision of LPTs performance and operability estimates. This issue, common in conventional turbomachinery, is also likely to challenge the design of future electric fans and propellers.

To improve the modeling of loss mechanisms and calibrate CFD transition models, experimental data are crucial. Research in this field is often conducted in linear cascades, which are a fundamental environment for studying turbomachinery flows [7]. In the past years, an extensive experimental campaign was conducted at the von Karman Institute to characterize the aerodynamics of the SPLEEN C1 cascade, a transonic low-pressure turbine geometry representative of the modern geared turbofan (GTF) architecture [8, 9]. High-speed (HS) cascade testing allows to recreate engine-relevant Reynolds and Mach numbers. However, it comes with drawbacks: a high-power compression system is required, making high-speed tests in closed-loop wind tunnels expensive. Additionally, the high flow speeds limit the temporal resolution of the measurements, thus increasing the complexity of the experiments. For these reasons, low-speed (LS) cascade testing remains valuable in fundamental research, despite the necessary compromises. To obtain detailed boundary layer data of the SPLEEN C1 blade and characterize its receptivity to varying free-stream turbulence levels, a follow-up experimental campaign is planned in a low-speed wind tunnel as part of the EU-funded HE-ART project.

This paper presents the cascade scaling methodology applied to the SPLEEN C1 cascade to achieve boundary layer similarity between high-speed and low-speed conditions. Due to the differing Mach number regime, full dynamic similarity with engine conditions cannot be established in low-speed flows. Therefore, modifications to the high-speed cascade are necessary to replicate loading and boundary layer characteristics in low-speed experiments. This work focuses on identifying and preserving the key parameters that influence the boundary layer and that can be maintained in low-speed flows, while also determining the necessary modifications to the high-speed cascade layout to account for compressibility effects. To inform the scaling process, a preliminary study was conducted on the parameters affecting boundary layers

---

*Corresponding author: giacomo.pastorino@vki.ac.be and blade loading across the two different flow regimes. The cascade redesign methodology is presented, detailing the low-speed scaled geometry and its comparison to the high-speed version. Additionally, the paper analyzes boundary layer evolution and profile losses for both high- and low-speed cascades. A qualitative overview of secondary flow patterns, including kinetic energy losses and turning angle, is provided for the two cascades, to highlight the impact of the scaling on this part of the flow field. This discussion identifies which aerodynamic and geometrical features can be preserved in low-speed cascades, compared to high-speed testing, along with the inherent limitations and the required modifications when significant Mach number reductions are imposed.

2 Scaling strategies

2.1 Scaling inputs and limitations

The SPLEEN C1 high-speed cascade models the rotor hub geometry of a geared low-pressure turbine, and was designed to operate in transonic Mach number regimes and at low Reynolds numbers. The high-speed cascade must be scaled for operation in a facility with an outlet Mach number of up to 0.1. Despite a wide range of high-speed Mach and Reynolds number combinations tested experimentally, the current objective is to replicate the boundary layer state observed under the high-speed design operating condition ($M_{2,is} = 0.9$, $Re_{2,is} = 70k$). Notably, despite reaching peak Mach numbers of ~ 1.1 on the suction side when operated at the nominal point, the high-speed cascade did not exhibit shock waves or shock-induced transition [10, 11], which would be impossible to replicate in low-speed flows. Similarly, base pressure losses, which can be significant in high-speed applications, cannot generally be replicated in low-speed testing [12]. However, when the boundary layer momentum thickness is sufficiently large relative to the trailing edge radius ($\Sigma\theta/R_{TE} > 4$), as in the present high-speed case, the base pressure term is expected to be negligible, with boundary layer losses being the dominant factor [13].

The absence of both shock patterns and significant base pressure effects allows for scaling the experiment to low-speed flows. To address the Mach number reduction, the low-speed scaling strategy focuses on maintaining as many critical flow and cascade parameters as possible in the low-speed experiments, while closely replicating the high-speed boundary layers. However, due to lost compressibility effects, the low-speed cascade cannot precisely replicate high-speed off-design conditions. The scaling process presented in this paper is tailored to match the boundary layer characteristics specifically for the design high-speed operating point, and replicating multiple off-design high-speed conditions would require different low-speed geometries for each case. Any other compressibility effects on the cascade aerodynamics that cannot be compensated for, if any, will be evaluated a posteriori and treated as limitations of low-speed cascade testing.

2.2 Boundary layer scaling

Replicating boundary layers and transition mechanisms similar to those encountered in high-speed blades is crucial for conducting meaningful low-speed experiments. It is well-established that factors such as Reynolds number, pressure gradients, and free-stream turbulence intensity significantly influence turbomachinery boundary layers [14, 15], and it is therefore critical to preserve these quantities also in low-speed experiments. Recently, there has been an increased focus on turbulence spectral distribution, i.e. the free-stream turbulence length scales [16–18]. Fransson and Shahinfar [17] argued that the transition process is modulated by the ratio of free-stream turbulence length scales to boundary layer thickness. To this end, both passive and, more recently, active turbulence grids have proven effective in tuning the free-stream turbulence to desired levels of intensity and scale [19, 20]. However, a key challenge remains: for a datum airfoil geometry, the pressure gradients encountered in high-speed conditions differ significantly from those in incompressible flows.

To ensure that low-speed cascades exhibit engine-representative pressure gradients, the aerodynamic scaling of the cascade is necessary to account for compressibility effects. Several authors have analyzed the aerodynamic scaling of low-pressure turbine cascades for low-speed testing, though from high-subsonic conditions. Vera and Hodson [21] scaled an LPT cascade to match the high-speed normalized velocity distribution. In their approach, the Reynolds number and exit flow angle were set equal to the high-speed values, while the inlet flow angle was adjusted accordingly. Marconcini et al. [7] performed three different scalings for the T106C blade, matching the pressure coefficient $C_p = \frac{p_{01}-p(s)}{p_{01}-p_2}$, the normalized isentropic Mach number $M_2/M_{2,is}$ and the normalized velocity distributions $v_2/v_{2,is}$ along the normalized blade surface length. Nine airfoil parameters and the pitch-to-chord ratio served as the degrees of freedom to modify the blade geometry. The authors concluded that the closest agreement with the separation bubble model of Hatman and Wang [22] and the high-speed kinetic energy losses was achieved by matching the C_p distribution. This approach preserved the same pressure gradient along the blade, a result not observed when Mach and velocity profiles were chosen as targets. In these last two cases, the flow was subjected to a higher diffusion rate affecting both boundary layer transition and the reattachment point. The scaled blade exhibited higher stagger and exit flow (+4 deg) angles and a slightly decreased pitch-to-chord ratio compared to the high-speed blade. Similarly, Giovannini et al. [23] applied the same approach to redesign a three-dimensional LPT blade for low-speed testing. Michálek et al. [24] carried out the low-speed redesign of the T108 cascade, maintaining the same inlet flow angle, but significantly increasing the stagger angle and the blade thickness. Similar observations can be found in the work of Houtermans et al. [25]: although no quantitative comparison between the high- and low-speed blades is provided, a visual inspection of the two cascades highlights a noticeable increase in both blade thickness and outlet flow angle for the low-speed case.

Based on the evidence in the available literature, matching the high- and low-speed C_p distribution was the approach chosen in this work, as it has proven to be the most effective way to preserve pressure gradients and boundary layer behavior on the blade surfaces. It is important to note, however, that this approach has demonstrated its validity for cascades with peak Mach numbers below 0.85, while the SPLEEN high-speed cascade reaches $M_{peak} \sim 1.1$. The remainder of this paper demonstrates that effective scaling can still be achieved under these conditions, provided no shock-induced phenomena are present. At the same time, the paper acknowledges the limitations of imperfect replication of compressibility effects on boundary layers, which are lost in the low-speed case. Regarding the other factors influencing the boundary layer state, the high-speed Reynolds number was maintained during scaling by adjusting the low-speed blade size and flow velocity, while free-stream turbulence intensity and scales will be controlled during the experiments using active turbulence grids.

2.3 Cascade geometry scaling

In Refs. [7] and [24], the Zweifel coefficient Zw was preserved. The Zweifel coefficient is a widely used parameter that provides an indication of turbine blade loading. It is defined as the ratio of the tangential force on a real blade to that on an ideal blade, where the flow is stagnated on the pressure surface and moves at the mean exit velocity on the suction surface [26]. The definition of the Zweifel coefficient is:

$$Zw = \frac{\oint p \, \mathrm{d}x}{C_{ax}\,(p_{01} - p_2)} \tag{1}$$

This formulation can be rearranged through a few mathematical substitutions, yielding the circulation of the C_p profile along the blade surface, normalized by the axial chord:

$$Zw = \oint C_p \, \mathrm{d}\left(\frac{x}{C_{ax}}\right) \tag{2}$$

As a consequence, one might think that matching the C_p profile would automatically ensure a match of the Zw coefficient. However, despite the similarity, the C_p profile was preserved differently in the two referenced works: in one case [7], it was preserved along the normalized surface length (s/s_L), while in the other [24], along the axial direction normalized by the chord (x/C_{ax}). For blades within the same family, with similar flow and stagger angles, and comparable thickness, the two approaches yield practically the same result; however, this is not universally applicable to all cases. Coull and Hodson [26, 27] argued that the Zweifel coefficient is not a universal representation of the blade loading, as it neglects blade camber, i.e., blade shape and curvature. To address this, they introduced the circulation coefficient C_0, defined as the ratio of the blade circulation to an ideal blade with stagnated flow on the pressure side and $v = v_2$ over the entire suction side:

$$C_0 = \oint \left(\frac{v}{v_2}\right) \mathrm{d}\left(\frac{s}{s_{L,ss}}\right) = \oint \sqrt{C_p} \, \mathrm{d}\left(\frac{s}{s_{L,ss}}\right) \tag{3}$$

Accounting for blade shape and curvature, the C_0 parameter is more general. Additionally, normalizing over surface length is particularly advantageous for boundary layer studies, as the true boundary layer development length is the blade surface and not the axial chord.

Despite these considerations, the scaling in this study was performed while keeping the blade within the same family, avoiding extreme alterations to the original shape. Therefore, the Zweifel coefficient still offers a meaningful way to perform a preliminary comparison of the loading profiles between high- and low-speed blades, despite differences in flow conditions. This is particularly valuable because the Zweifel coefficient can be expressed in terms of key physical quantities that directly influence blade loading [7]:

$$Zw = \frac{\gamma \mathrm{M}_{2,is}^2 \cos^2\alpha_2 \left(\frac{\rho_{2,is}}{\rho_1}\tan\alpha_1 + \tan\alpha_2\right)}{\left[\left(1+\frac{\gamma-1}{2}\mathrm{M}_{2,is}^2\right)^{\frac{\gamma}{\gamma-1}} - 1\right]} \frac{g}{C_{ax}} \tag{4}$$

This formulation is highly convenient, as it highlights the key flow parameters that impact the blade loading, namely inlet and outlet flow angles α_1 and α_2, the isentropic Mach number, the density ratio $\rho_{2,is}/\rho_1$ and the pitch-to-axial chord ratio g/C_{ax}. In low-speed flows, the effects of Mach number and density ratio are negligible. Therefore, by calculating the Zweifel coefficient for the high-speed blade and maintaining it constant for the low-speed case, the designer can explore various ranges of flow angles and pitch-to-chord ratios in low-speed conditions to achieve the target Zweifel coefficient. A comparison of the estimated Zweifel coefficient computed at high- and low-speed conditions is reported in Fig. 1.

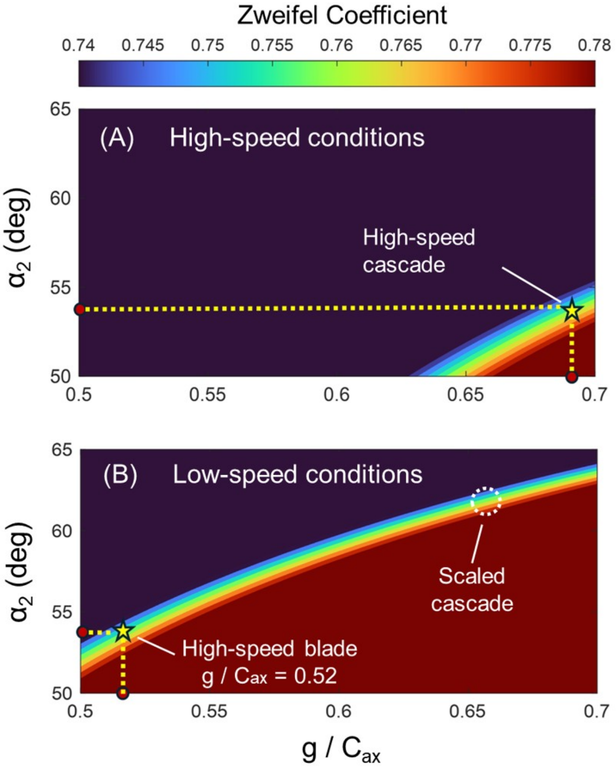

Figure 1: Zweifel coefficient contour as a function of outlet flow angle and pitch-to-axial chord ratio. (A): High-speed conditions $M_{2,is} = 0.9$ (B): Incompressible flow regimes.

To generate this plot, the inlet flow angle was fixed to the nominal inlet angle of the high-speed SPLEEN cascade, $\alpha_1 = 37.3$ deg, while the pitch-to-axial chord ratio and the outlet flow angle were varied. The colormap is intentionally saturated to emphasize a narrow band around the high-speed Zweifel number. For the SPLEEN high-speed cascade, the pitch-to-axial chord ratio is $g/C_{ax} = 0.692$, and the outlet angle $\alpha_2 = 53.8$ deg. The resulting Zweifel coefficient computed with Eq. 4 is $Zw = 0.762$. The position of the high-speed cascade in the Zweifel plot is highlighted with a star marker in Fig. 1(A). When transitioning to low-speed conditions, the impact of compressibility becomes evident, shifting the iso-Zweifel lines from the bottom right of Fig. 1(A), corresponding to high pitch and small outlet angle, to regions with lower pitch and higher outlet angles in Fig. 1(B).

To replicate similar secondary flows between high- and low-speed cascades, it is ideal to maintain the same flow angles. By fixing α_1 to the high-speed value, Eq. 4 was used to determine the g/C_{ax} that ensures the high-speed values of α_2 and Zw are matched under low-speed conditions. The required pitch-to-axial chord ratio is $g/C_{ax} = 0.52$, as indicated by the star marker in Fig. 1(B). Under the assumption that maintaining the high-speed blade geometry in low-speed conditions would result in comparable high- and low-speed outlet flow angles, an initial scaling attempt was made by setting $g/C_{ax} = 0.52$, without altering the original blade shape. The resulting C_p profile, plotted in Fig. 2 in blue, is compared against the target high-speed distribution (black line). For reference, the C_p profile of the original high-speed cascade operated at low-speed conditions is also shown in red. Evidently, the loading of the high-speed cascade, when operated under low-speed conditions, deviates significantly from the target high-speed load, both in terms of the suction side peak location and lift. This scenario corresponds to the bottom right of Fig. 1(B), where Zw is notably higher than the target value, due to the increased lift. When g/C_{ax} is reduced to 0.52, Zw remains consistent with the target blade, indicating that the area enclosed by the target and scaled C_p curves is similar. The outlet flow angle also closely matches the high-speed value — 53.4 deg and 53.8 deg for LS and HS cascades, respectively. However, significant differences remain in the pressure distribution along the suction and pressure surfaces.

These observations led to several important conclusions. First, matching the Zweifel coefficient alone is not sufficient to replicate the C_p profile of a reference blade, even for blades within the same family. Second, if the inlet and outlet angles are fixed, simply adjusting the cascade pitch does not allow to achieve the same C_p distribution at high- and low-speeds conditions, meaning the same pressure gradients on the blades cannot be attained. Therefore, some constraints must be relaxed, and the cascade must be scaled by modifying the blade shape and/or increasing the outlet flow angle.

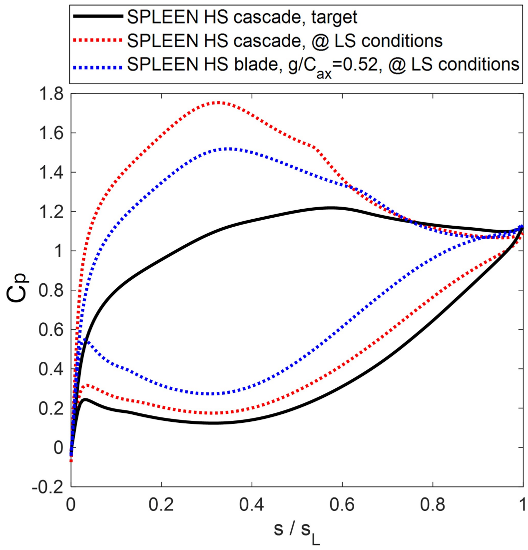

Figure 2: High-speed blade C_p profiles: nominal conditions (black), LS conditions (red), and with $g/C_{ax} = 0.52$ (blue).

3 Blade redesign

To efficiently perform the scaling, the blade geometry was parameterized and optimized. In each iteration, a new geometry was generated, and the C_p distribution was computed using the MISES cascade solver [28, 29]. The objective function to be minimized was the difference between the newly computed C_p distribution and the target high-speed distribution:

$$f = \sqrt{\frac{1}{N}\sum_{i=1}^{N}\left[C_{p,New}(i) - C_{p,Target}(i)\right]^2} \tag{5}$$

with the index i representing the number of nodes used to discretize the blade loading. Starting with a coarser node count in the initial redesign, this number was progressively increased to 200 in the final optimization step to smoothly describe the C_p profile.

3.1 MISES validation

Before scaling the blade, the MISES solver was tested to evaluate its ability to accurately resolve the original SPLEEN C1 cascade at nominal conditions. MISES is a coupled viscous-inviscid solver that uses steady Euler equations to solve the flow, while modeling the boundary layer through integral equations. The two domains are coupled using the Newton-Raphson method. A modified version of the Abu-Ghannam/Shaw transition model [30] is implemented in the code [31]. Figure 3 displays a comparison between experimental data, presented by Lopes et al. [32], and MISES results. The computation was performed at nominal conditions of $M_{2,is}$=0.9 and $Re_{2,is}$=70k, with turbulence set to the experimentally measured value.

The comparison demonstrated a high degree of agreement between the experimental data and MISES predictions. This satisfactory match confirmed MISES as a reliable tool to estimate blade loading characteristics, leading to its selection for the scaling and optimization tasks due to its efficiency and accuracy. It proved to be highly effective for optimization purposes, allowing for the execution of thousands of simulations within a few hours and enabling rapid optimization of the blade design.

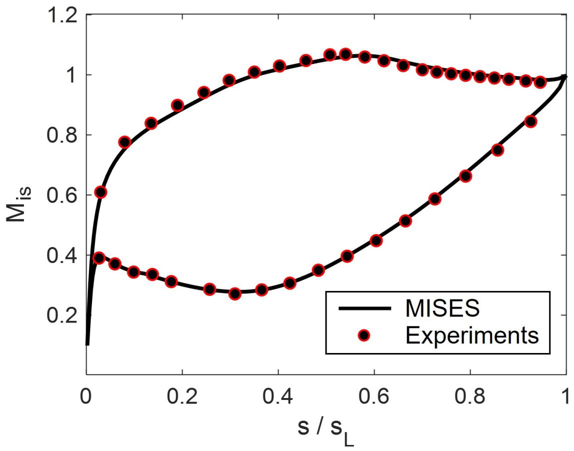

Figure 3: Comparison between the isentropic Mach number profiles obtained with MISES and experimental data [32].

3.2 Airfoil parametrization

A well-defined parameterization of the cascade and a proper choice of the optimization variables is essential to achieve effective optimization. A parameterization capable of accurately reproducing the original high-speed geometry was chosen, based on the assumption that this approach would also be suitable for low-speed blades with similar shapes and characteristics. First, a camber line was defined using the inlet and outlet metal angles, along with the stagger angle. The blade coordinates were normalized along the axial direction, setting the camber line endpoints at (0, 0) and (1, $tan(\gamma)$). To ensure tangency at the endpoints and match the desired inlet and outlet metal angles, two additional constraints were adopted. These constraints impose that the derivatives at the endpoints correspond to the tangents of the inlet and outlet metal angles, $tan(\alpha_{1,m})$ and $tan(\alpha_{2,m})$, as shown in Fig. 4. A cubic function was used, as it is uniquely determined by the two endpoints and their derivatives. This polynomial function was chosen because it is based on physical parameters and guarantees C^2 continuity across the blade profile. Thickness elements, represented by weighted Bernstein polynomials, were then added to both sides of the camber line to create independent pressure and suction surfaces. A common thickness element at the leading edge ensures continuity between the pressure and suction surfaces at this critical point. This methodology, based on an airfoil parametrization by Kulfan [33], was then employed by Clark [34] to populate a database of high-pressure turbines with various geometries. Following Clark guidelines, specific precautions were also taken to ensure smooth airfoil characteristics, prevent nonphysical shapes and achieve the desired trailing edge thickness. The comparison between the original high-speed cascade and the parameterized blade, shown in Fig. 4(A), demonstrates a high degree of fidelity. Additionally, Fig. 4(B) shows excellent agreement in blade curvature (K), with minor discrepancies at the leading edge due to the lower node density in the original blade, which affects curvature estimation in a region with rapid geometrical variation. Together, these results validate the suitability of this parameterization for low-pressure turbine blades. The curvature of the scaled low-speed blade, plotted in green in Fig. 4(B), is discussed later in Sec. 4.1.

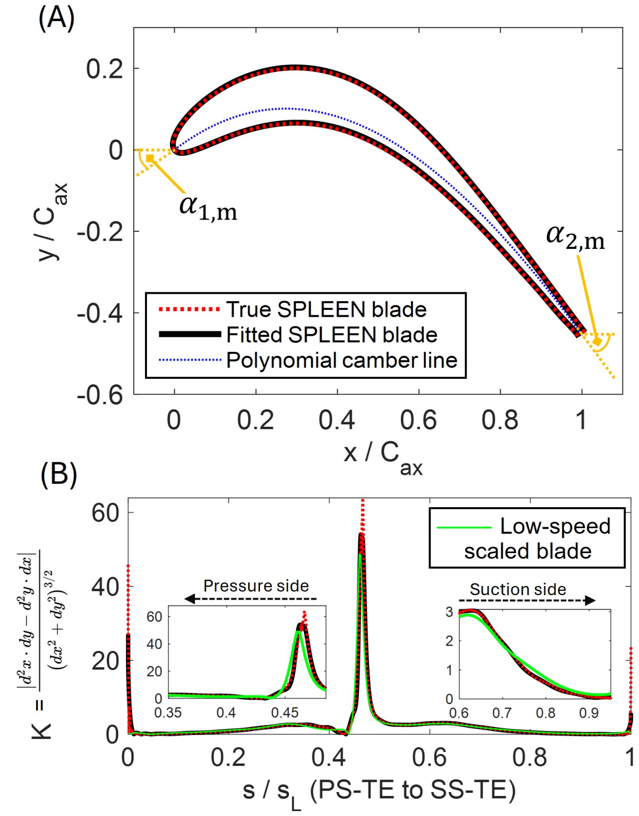

Figure 4: Comparison of the true SPLEEN blade (red) and its parametric representation (black): (A) Geometric layout, showing the polynomial camber line (blue) and its tangency to the metal angles (orange), and (B) blade curvature, with the scaled low-speed blade plotted in green.

3.3 Computational Framework: Optimization, Constraints, and Boundary Conditions

The optimization was performed using the Nelder-Mead algorithm, also known as the *simplex method*. During the process, the design variables were the weights of the Bernstein polynomials, defining the blade thickness, and the pitch-to-chord ratio. Preliminary optimizations used a low variable count to generate an initial cascade layout. The number of variables was progressively increased, and the final geometry was parametrized with 50 variables (24 SS-modes, 24 PS-modes, pitch-to-chord ratio, and the leading edge mode), providing a balance between replicating high-speed loading while avoiding unacceptable waving blade shapes. Since the parameterization does not allow direct control over blade thickness, penalties were applied by adding a large constant to the objective function to discard airfoils that were too thick or too thin, ensuring consistency with the high-speed blade family and avoiding manufacturing issues. The original high-speed blade features $t_{max}/C_{ax} = 0.135$, and the penalty strategy was employed to force the low-speed blade t_{max}/C_{ax} between 0.12 and 0.19. Additionally, the trailing-edge radius was constrained to remain within a range close to that of the high-speed blade. Following the procedure in Refs. [7, 24], the inlet flow angle was fixed at the high-speed value, while the outlet flow angle was not predetermined or constrained; it was treated as a degree of freedom and thus became a result of the optimization process.

Regarding the boundary conditions, the inlet turbulence intensity was set to 2.5%, but the transition was tripped at the high-speed locations ($x/C_{ax} = 14\%$ and 90% for PS and SS, respectively) to avoid any bias induced by the AGS model. The outlet isentropic Mach number was fixed at $M_{2,is} = 0.051$, and the inlet Reynolds number was set to Re_1=47k, matching the inlet conditions of the SPLEEN high-speed cascade. This set of constraints ensured similar boundary layer receptivity at the leading edge, at the expense of a slightly higher $Re_{2,is}$ compared to the high-speed value.

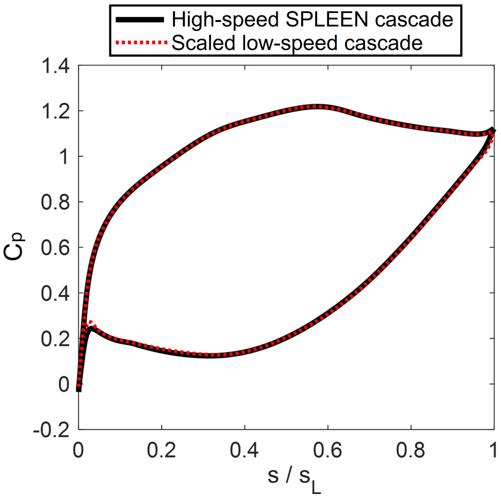

Figure 5: C_p distributions of the original high-speed SPLEEN blade and the scaled one for low-speed testing.

4 Results and discussion

4.1 Cascade layout

Initial scaling attempts were conducted by maintaining the same stagger angle of the high-speed blade; however, the match of the target loading was unsatisfactory. Consequently, the blade stagger angle was increased to 28.4 deg, a 4-degree increment, following the methodology outlined in Refs. [7, 24]. Additionally, the trailing edge thickness was slightly enhanced to improve the loading match near the trailing edge. As shown in Fig. 5, these adjustments allowed the optimizer to identify a blade that perfectly matched the desired pressure distribution.

Figure 6(A) compares the normalized low- and high-speed geometries, highlighting the increase in both stagger and outlet angles for the low-speed blade. In Fig. 6(B), the thickness distribution is shown. Starting from the true blade mean line, the thickness was defined as the distance between the pressure and suction sides, measured by perpendicular segments extending from the mean line to both sides. The low-speed blade is overall thicker, with an increase in maximum thickness (t_{max}/C_{ax}) of approximately 13.3%. Figures 6(C) and (D) compare the full passages of the high- and low-speed blades, along with relevant geometrical quantities. The pitch-to-axial chord ratio was reduced by 5%, resulting in $(g/C_{ax})_{LS} = 0.658$. Regarding the blade shape, the rear suction side, originally straight, exhibits increased curvature in the low-speed blade, with the rear suction side turning angle (ε_{SS}) doubling from 4.7 deg to 9.4 deg. However, as seen in Fig. 4(B), this difference remains relatively small and only becomes noticeable when zooming into the right subplot. A similar observation applies to the pressure side, where both trends and quantitative values are comparable, with minor differences primarily occurring near the leading edge ($s/s_L \approx 0.35$ to 0.5). Given the minor influence of curvature on bound-

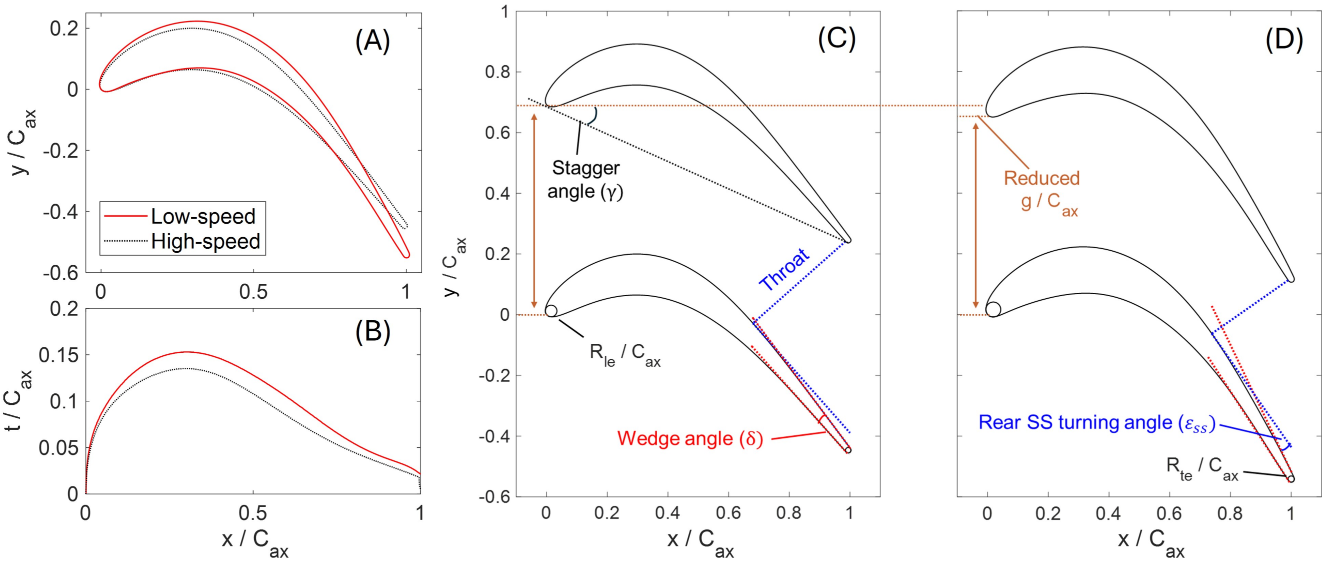

Figure 6: Comparison between the high- and low-speed blades: (A) High- and low-speed single airfoils, (B) thickness distributions, (C) full high-speed passage, and (D) full low-speed passage. Relevant geometrical quantities highlighted in (C) and (D).

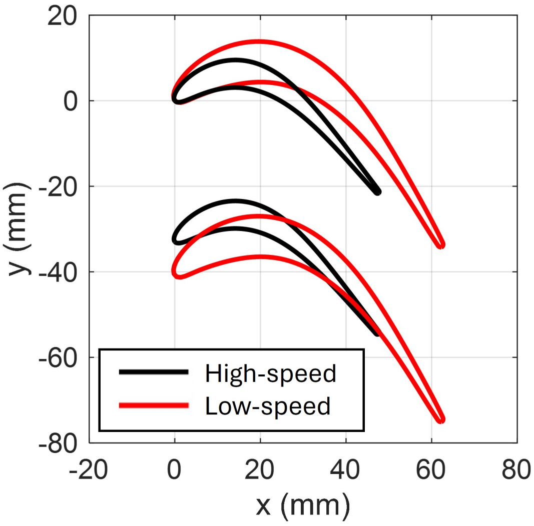

Figure 7: Cascade passages, to scale. Geometries in mm.

ary layer behavior [14, 35], such small variations between the high- and low-speed designs are not expected to significantly affect the boundary layer state. Due to the increased stagger angle and reduced pitch-to-chord ratio, the throat length (o/C_{ax}) was significantly reduced, with a decrease of approximately 25% in the low-speed cascade. The leading edge radius (R_{LE}/C_{ax}) was increased by 28.8% in the low-speed cascade. Additionally, as mentioned earlier, the trailing edge thickness was slightly increased to better match the trailing edge load, resulting in a 13% increase in the trailing edge radius of the low-speed blade. Considering the design Reynolds number and fixing the static pressure downstream to ambient conditions, the axial chord of the scaled blade was determined to be $C_{ax,LS}$ = 62.1 mm — significantly larger than $C_{ax,HS}$ = 47.6 mm. This size increase is beneficial to improve the measurement spatial resolution. Fig. 7 illustrates the two cascade passages to scale, showing their true size for comparison. This blade was designed for a linear cascade with a maximum span of h=127 mm. This design was validated through three-dimensional RANS simulations, discussed in a later section, to ensure an axial velocity density ratio close to 1 and two-dimensional flow at midspan.

The outlet flow angle $\alpha_{2,LS}$, left unconstrained during the optimization process, was a result of the scaling and, together with the pitch-to-chord ratio, one of the two factors influencing the cascade Zweifel coefficient. The value computed by MISES for the low-speed design is 61.5 deg, marking an increase of approximately 14.3% compared to the high-speed blade. This result suggested that to match the target pressure distribution in low-speed conditions, adjustments are required in both the outlet flow angle and the pitch-to-chord ratio. The scaled blade design can be located near the top-right corner of the Zweifel contour plot in Fig. 1(B), where it is indicated by a white dashed circle, significantly distant from the initial scaling guess where only the pitch-to-chord ratio was modified. The Zweifel coefficient, computed with Eq. 1, is $Zw_{LS} = 0.758$ and $Zw_{HS} = 0.742$ for the low- and high-speed cascades, respectively. These values are similar to each other and close to those predicted by Eq. 4. The C_0 coefficient for the low-speed cascade is $C_{0,LS} = 0.530$, compared to $C_{0,HS} = 0.524$. The close match of both coefficients in both high- and low-speed configurations supports the earlier explanation: when significant variations in angles and shapes are not anticipated (e.g., during high-to-low-speed scaling), both Zw and C_0 provide similar information. In this sense, Zw remains a useful parameter for preliminary design choices, as indicated by Eq. 4.

The main flow and geometrical parameters for the high- and low-speed cascades are summarized in Table 1.

Table 1: Main flow and geometrical parameters for the high-speed and scaled cascade.

Quantity	Low-speed	High-speed	Unit
$M_{2,is}$	0.0511	0.900	[-]
$Re_{2,is}$	80k	70k	[-]
Re_1	47k	47k	[-]
α_1	37.0	37.3	[deg]
α_2	61.5	53.8	[deg]
γ	28.4	24.4	[deg]
C_{ax}	62.1	47.6	[mm]
C	70.9	52.3	[mm]
g/C_{ax}	0.658	0.692	[-]
Zw	0.758	0.742	[-]
C_0	0.530	0.524	[-]
t_{max}/C_{ax}	15.3	13.5	[%]
R_{LE}/C_{ax}	2.46	1.91	[%]
R_{TE}/C_{ax}	1.02	0.90	[%]
o/C_{ax}	0.307	0.407	[-]
δ	7.4	4.9	[deg]
ε_{ss}	9.4	4.7	[deg]

4.2 Boundary layers

A comparison between the high- and low-speed transitional boundary layer parameters computed by MISES is shown in Fig. 8. The first subfigure 8(A) illustrates a strong similarity in the displacement thickness, normalized by the axial chord, δ^*/C_{ax}, on the pressure surface between the high- and low-speed blades. Similar qualitative trends are evident on the suction side; however, the high-speed blade shows a larger displacement thickness per unit chord length, reaching up to 30% higher at its maximum value. This result implies that δ^*/C_{ax} cannot be preserved, especially on the suction side. While no specific scaling rules for displacement thickness from high- to low-speed conditions were found in the literature, this result indicates that matching C_p yields good agreement in δ^*/C_{ax} on the pressure side, where the flow in the original blade is slower and less influenced by compressibility effects. However, on the suction surface, scaling down to incompressible regimes by matching C_p may not reproduce identical boundary layer blockage. In contrast, the agreement between the high- and low-speed cascades in terms of θ/C_{ax} is remarkable on both surfaces, as shown in Fig. 8(B).

To validate the trends observed on the suction side, additional two-dimensional RANS simulations were performed

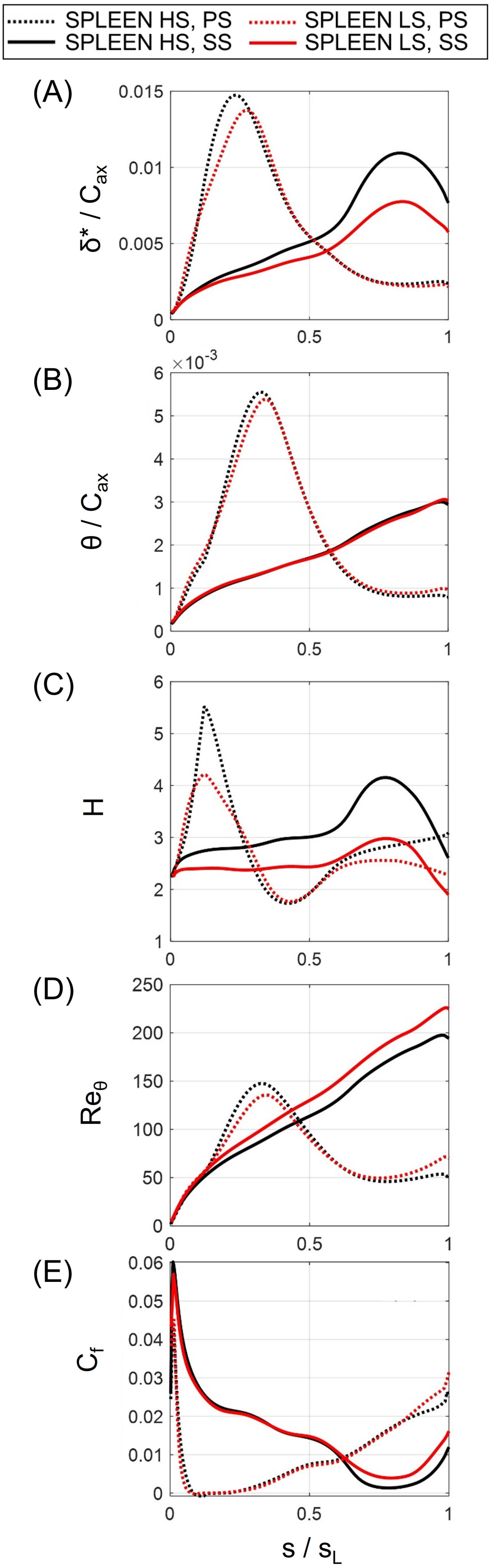

Figure 8: Boundary layer parameters for high- and low-speed blades.

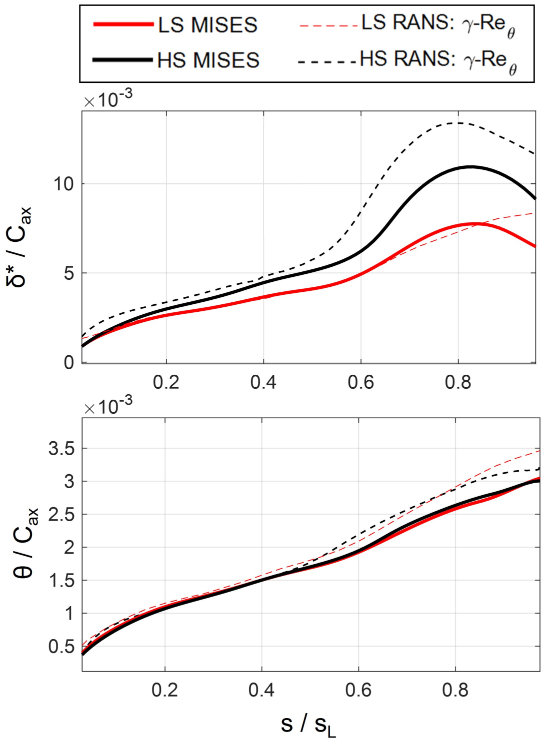

Figure 9: Displacement and momentum thickness plots for the high- and low-speed blades suction side, comparing MISES and CFD results. High-speed CFD results from Ref. [10].

using *Cadence FINE/Turbo 18.2* with the $\gamma - Re_\theta$ transition model by Langtry and Menter [36]. The boundary layer profiles extracted from these simulations were compared to both the MISES results and the high-speed RANS simulation performed by Lopes [10]. In Fig. 9, both displacement and momentum thickness profiles from RANS and MISES are plotted. The values of δ^*/C_{ax} from RANS are qualitatively consistent with the MISES computations, with an even greater difference between the high-speed and low-speed profiles. Despite quantitative differences, which may be attributable to the different transition models and would require experimental data for a more precise analysis, this observation confirms that when scaling by matching C_p, the displacement thickness—and consequently the boundary layer blockage effect—is expected to be higher in high-speed conditions. On the other hand, the agreement between the momentum thickness computed by RANS and MISES is remarkable: RANS results are slightly higher, but the θ/C_{ax} trends are again closely matched between the two blades. This analysis suggests that matching C_p allows to scale to low-speed the boundary layer momentum loss.

The shape factor, defined as $H = \delta^*/\theta$ is plotted in Fig. 8(C). Due to its direct dependence on δ^*, similar observations to the ones made for the displacement thickness can be drawn. Qualitative trends are similar between high- and low-speed cascades, with better agreement on the pressure surface. However, due to discrepancies in displacement thickness on the suction surface, the low-speed blade exhibits a significantly smaller shape factor. The high-speed blade appears to operate at an incipient state of separation ($H_{max} \sim 4$), while the low-speed blade remains further from separation.

The momentum thickness Reynolds number Re_θ is shown in Fig. 8(D). The plot highlights similar trends on both surfaces for both blades. Again, a closer agreement is observed on the pressure surface, while on the suction side, the low-speed blade exhibits a higher Re_θ, with a maximum increase of $\Delta Re_\theta \sim 25$ close to the trailing edge.

Lastly, Fig. 8(E) presents the skin friction coefficient (C_f) trends, which show good qualitative and quantitative agreement between the two flow conditions. A similar matching of high- and low-speed C_f was reported by Marconcini et al. [7] for the T106C cascade, though in the presence of a significant separation bubble. The main differences between high- and low-speed blades appear in the rear portion of the suction side, where the high-speed C_f is nearly tangent to zero, suggesting, as previously noted, that the high-speed blade is closer to incipient separation than the low-speed one. Nevertheless, MISES predicts that the flow remains attached for both blades. It is worth noting that for the high-speed SPLEEN cascade, it was not possible to conclusively identify suction side separation from MISES results by examining the skin friction coefficient alone. Separation was observed experimentally by Lopes [10] using other methods based on the Thwaites parameter, suggesting that even if C_f does not become negative in the simulations, this does not necessarily imply the absence of a separation bubble.

To conclude this section, despite matching qualitatively and quantitatively all BL parameters on the pressure side, and θ/C_{ax} on the suction side, the low-speed blade operates with a lower shape factor and a slightly higher skin friction coefficient on the rear portion of the suction side. Therefore, the similarity with respect to the high-speed suction side boundary layer achieved in terms of BL momentum loss, but the high-speed blade is closer to separation compared to its low-speed counterpart. This novel observation, not reported in previous scaling studies, may highlight a limitation when scaling a transonic blade without a significant separation bubble to low-speed conditions by solely matching the high-speed pressure distribution. While not explicitly covered in this work, an alternative scaling strategy prioritizing the matching of boundary layer parameters, such as shape factor or skin friction coefficient, at the expense of a mismatch on the pressure distribution, might allow for a more comprehensive boundary layer similarity.

4.3 Profile losses

Different methods are used to quantify the profile loss generated by a cascade. Losses are typically categorized into total pressure losses and kinetic energy losses; however, kinetic energy loss is often preferred due to its insensitivity to compressibility [37]. The kinetic energy loss coefficient is defined as:

$$\xi = 1 - \frac{1 - \left(\frac{p_2}{p_{02}}\right)^{\frac{\gamma-1}{\gamma}}}{1 - \left(\frac{p_2}{p_{01}}\right)^{\frac{\gamma-1}{\gamma}}} \tag{6}$$

For a cascade with a sufficiently high aspect ratio, the primary contributor at midspan is the profile loss. Kinetic energy profile losses calculated by MISES are ξ_{LS} = 4.37% and ξ_{HS}= 3.25% for the low-speed and the high-speed cascades, respectively. To explain this difference, it is useful to identify the parameters influencing profile losses. Cadrecha and Vázquez [38] highlighted momentum thickness, outlet flow angle, and cascade pitch as key contributors:

$$\xi \sim \frac{2\theta_{TE}}{g\cos\alpha_2} = \frac{2(\theta_{TE}/C_{ax})}{(g/C_{ax})\cos\alpha_2} \tag{7}$$

While this is an approximation, it is interesting to notice that a similar term appears in Denton's well-known equation [39] for estimating profile total pressure losses:

$$\omega = \left(\frac{-C_{pb}t_{TE}}{g\cos(\alpha_2)}\right) + \left(\frac{\sum\delta^*_{TE} + t_{TE}}{g\cos(\alpha_2)}\right)^2 + \left(\frac{2\sum\theta_{TE}}{g\cos(\alpha_2)}\right) \tag{8}$$

where the first term represents the base pressure loss, the second the blockage effects, and the third the boundary layer momentum deficit. According to Coull and Hodson [1], the boundary layer momentum deficit contributes around 90% of the total loss, making it the primary focus of the following analysis. In Eq. 7, the numerator is the same between the two cascades, since θ/C_{ax} is conserved, as previously shown in Fig. 8(B). The difference in losses must then be imputed to the denominator, which depends purely on the geometry of the two cascades. The term $(g/C_{ax})\cos(\alpha_2)$ can be interpreted as the discharge area of the cascade passage, where the boundary layer mixes with the main flow, and it is approximately equal to the cascade throat o. By computing the ratio o_{LS}/o_{HS}, a factor of 0.75 is obtained, identical to the ratio of ξ_{HS}/ξ_{LS}. This observation reveals that two concurrent factors contribute to the higher overall losses in the scaled low-speed blade: a reduction in the pitch-to-axial chord ratio, g/C_{ax}, and an increase in α_2, both of them decreasing the denominator in Eq. 7. Recently, Senior and Miller [40] proposed a new model, validated for both high- and low-speed cascades. While similar to Denton model, it further develops the existing terms and introduces a fourth term accounting for trailing edge wedge-induced losses. Applying this model results in $\xi_{LS,SM}$ = 3.96% for the low-speed cascade and $\xi_{HS,SM}$ = 3.21% for the high-speed cascade. In both cases, momentum thickness-related terms account for about 66% of the total losses, making them the dominant contributor. The low-speed blade features lower blockage due to a smaller displacement thickness, see Fig. 8(A), but higher wedge angle losses. Both cascades show negligible base pressure losses, confirming the observations of Sect. 2.1. Overall, although the high-speed blade continues to exhibit lower losses, the loss ratio has slightly shifted to $\xi_{HS,SM}/\xi_{LS,SM}$ = 0.81, compared to the factor 0.75 previously observed and based solely on geometrical observations. The losses computed by MISES and with the Senior and Miller model are summarized in Table 2.

Several important conclusions can be drawn. First, as highlighted by previous authors, the momentum thickness loss is the dominant term in profile losses. Moreover, the profile loss does not depend only on the boundary layer thickness, but also on the discharge area $(g/C_{ax})\cos(\alpha_2)$. In this sense, having similar momentum thickness development along the blade

Table 2: Losses computed with MISES and with S&M model [40] for high- and low-speed cascades.

Quantity	Low-speed	High-speed	HS-LS Ratio
ξ_{MISES}	4.37%	3.25%	0.75
ξ_{SM} [40]	3.96%	3.21%	0.81

does not necessarily imply similar losses: in the current scaling, the reduction of the pitch-to-axial chord ratio and the increase of the outlet flow angle resulted in a smaller discharge area, therefore higher losses. This observation is not coincidental; it can be generalized by examining the Zweifel contour plot in Fig. 1 and the assumptions made to generate it. If the inlet flow angle is fixed to the high-speed value, and the Zweifel coefficient is matched by conserving the C_p distribution, achieving the same profile losses becomes impossible. When θ/C_{ax} is matched between the HS and LS blades, maintaining the same profile losses would require the term $g/C_{ax}\cos(\alpha_2)$ to be matched as well, as indicated by Eq. 7. However, Fig. 1(B) shows that to preserve Zw in low-speed flows, g/C_{ax} must decrease, and α_2 must increase. These changes both concur to a smaller $g/C_{ax}\cos(\alpha_2)$ in the low-speed case, which consequently leads to higher profile loss. Although beyond the scope of this paper, one possible solution for a designer aiming to match the profile loss between high- and low-speed conditions could be to perform a different scaling, matching C_p by modifying the inlet angle while attempting to preserve similar outlet angles and pitch-to-chord ratios.

4.4 Scaling effects on secondary flows and axial velocity density ratio

Three-dimensional RANS simulations were carried out using *Cadence FINE/Turbo 18.2*. The objectives were twofold: first, to validate the design choice of the chord size by verifying that the aspect ratio of the scaled blade is sufficiently high to ensure 2D flow at midspan and axial velocity density ratio (AVDR) close to 1. Second, the analysis aimed to estimate the effect of the scaling on secondary flow structures when transitioning from high- to low-speed conditions. To facilitate comparison, a fictitious high-speed case was generated with the same aspect ratio as the low-speed cascade, allowing for an analysis of the secondary flow penetration and structure across both regimes. Given the sensitivity of secondary flow structures to spanwise discretization, this study provides primarily qualitative rather than quantitative insights. However, to minimize mesh-related discrepancies, a similar mesh was used for both cases, consisting of 7.6M nodes for the high-speed blade and 6.8M nodes for the low-speed blade. A spanwise discretization of 205 streamlines, selected after a mesh sensitivity study, was employed for both cascades. The grid was generated with *Autogrid 5*. The y+ value was found to be consistently lower than 1 on both the endwalls and blade surfaces. Both simulations were run with the *k-ω SST* turbulence model, with fully turbulent boundary layers. For both cascades, α_1 was set to the nominal value and Re_1=47k. The domain inlet was placed three low-speed blade axial chords ($C_{ax,LS}$) upstream of the leading edge. In the absence of experimental inlet endwall BL profiles near the cascade leading edge, this choice simulates a BL suction system that will be placed approximately three chords upstream in the actual tests. This setup ensures similar endwall BL development for both simulated cases, due to the same inlet Reynolds number and development length.

The AVDR of the low-speed cascade was determined to be 1.005. Figure 10 highlights (A) the pitchwise-averaged values of deviation $\alpha_2 - \alpha_{2,MS}$ and (B) the secondary kinetic energy loss coefficient computed by assuming profiles loss constant along the span and equal to the midspan value ($\xi - \xi_{MS}$). Data were extracted at a plane located $0.5 \cdot C_{ax}$ downstream of the cascade outlet.

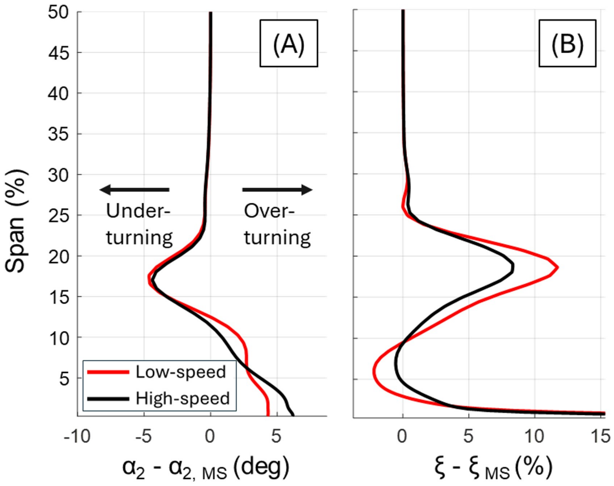

Figure 10: Secondary flow patterns: (A) Deviation from primary flow direction and (B) kinetic energy loss ($\xi - \xi_{MS}$).

It can be observed that both cascades maintain two-dimensional flow from midspan down to approximately 30% of the span, with the profiles overlapping, indicating that secondary flows do not penetrate further towards midspan. On one hand, this observation demonstrates that roughly 40% of the total span remains unaffected by secondary flows, confirming that the chosen aspect ratio of 1.8 is sufficiently high. On the other hand, it implies that with a similar inlet endwall boundary layer and same aspect ratio, the high-to-low-speed scaling is not expected to significantly impact secondary flow penetration. The flow deviation profile in Fig. 10(A) shows similar patterns between the high-speed and low-speed cascades in the core of the secondary flow, between 12 and 25% span, with a maximum under-turning between 4 - 5 deg for both cascades. In the over-turning region, the high-speed cascade shows greater turning from the endwall to 6% span, after which the trend reverses. The secondary kinetic energy loss for both high- and low-speed cases, shown in Fig. 10(B), exhibits again comparable patterns. However, the low-speed cascade shows a peak loss of approximately 12% in the core of the secondary flow, while the high-speed cascade peak loss is around 8%. This difference can be attributed to the greater flow turning in the low-speed case, as well as the relatively larger size of the secondary flow structures in the low-speed cascade compared to the cascade discharge area. It is worth noticing that the ratio of losses between the two cascades, previously observed in the midspan analysis to be around 0.75, holds true in the full-span case as well, with a ratio of secondary losses equal to 0.76.

5 Conclusions

In low-speed turbomachinery experiments, replicating boundary layer development and transition mechanisms as closely as possible to those in high-speed flows is crucial. While parameters such as Reynolds number and free-stream turbulence can be adjusted using turbulence grids or by modifying flow conditions and blade size, preserving the pressure distribution requires scaling the cascade geometry. This paper presented a redesign methodology to scale a high-speed LPT turbine cascade for low-speed testing, along with a comparison of the geometrical features, boundary layer characteristics, and performance parameters of the high- and low-speed cascades. The main findings of this investigation are summarized below:

- When scaling a high-speed cascade to low-speed conditions, the Zweifel coefficient (as expressed in Eq. 4) enables the designer to identify the cascade parameters that need to be adjusted to account for compressibility effects. Based on the results presented, both the pitch-to-chord ratio and the cascade turning must be modified.
- To match the target C_p, the cascade layout was optimized using a gradient-free method coupled with the MISES 2D cascade solver, while preserving the design inlet flow angle of the high-speed case. The optimized blade showed increased stagger and outlet flow angles, a higher overall thickness, and a reduced pitch-to-chord ratio compared to its high-speed counterpart. These trends align with those observed in previous studies.
- High- and low-speed normalized momentum thickness exhibited similar qualitative and quantitative trends. The normalized displacement thickness also showed similar trends on the pressure side, but was up to 30% larger on the suction side for the high-speed blade. The displacement thickness reduction lowered the shape factor in the low-speed case, indicating that the low-speed blade operates further from separation compared to its high-speed counterpart. This discrepancy may stem from compressibility effects influencing boundary layer blockage on the suction side, and suggests that while matching high- and low-speed C_p aligns the boundary layer momentum loss, it can still lead to different boundary layer states. To compensate this trend, an alternative scaling approach could be directly matching high- and low-speed boundary layer parameters, such as C_f or H, at the cost of a mismatch in the C_p profile.
- Matching the same momentum loss thickness is not sufficient to guarantee identical profile loss between the high- and low-speed configurations. The profile loss is also influenced by geometrical features, particularly the size of the discharge area where the boundary layer mixes with the main flow, which roughly corresponds to the passage throat for a 2D cascade. In this study, the reduction in pitch-to-chord ratio and increase in outlet flow angle in the low-speed cascade led to a smaller throat ($o_{LS}/o_{HS} = 75\%$), which in turn resulted in an increase in the low-speed profile loss ($\xi_{HS}/\xi_{LS} = 75\%$).
- A qualitative analysis of the secondary flow development highlighted that the chosen aspect ratio of 1.8 is sufficient to achieve two-dimensional flow at midspan, with secondary flow penetration limited to the first 30% of the span. Both high- and low-speed cascades exhibited similar deviations from the primary flow direction. However, the kinetic energy loss attributable to secondary flows is higher in the low-speed case.

Acknowledgements

This research has been performed in the framework of the HE-ART project (Hybrid Electric propulsion system for regional AiRcrafT), supported by the Clean Aviation Joint Undertaking and its members, and funded by the European Union's Horizon Europe research and innovation programme under the grant agreement No. 101102013. The authors also thankfully acknowledge Prof. Sergio Lavagnoli, Gustavo Lopes and Peter Cassidy for the support and the fruitful discussions.

Nomenclature

C, C_{ax}	Chord, axial chord
C_0	Circulation coefficient
C_f	Skin friction coefficient
C_p	Pressure coefficient
C_{pb}	Base pressure coefficient
g	Cascade pitch
H	Shape factor
h	Cascade span
K	Curvature
M	Mach number
o	Cascade throat
p	Pressure
R	Radius
Re	Reynolds number
s	Curvilinear abscissa
s_L	Surface length
t	Thickness
v	Velocity
x	Axial direction
y	Pitchwise direction
Zw	Zweifel coefficient

Greek symbols

α	Flow angle
δ	Wedge angle
δ^*	Displacement thickness
ε_{SS}	Rear suction side turning angle
γ	Stagger angle; ratio of specific heat
ρ	Density
ξ	Kinetic energy loss coefficient
θ	Momentum thickness
ω	Total pressure loss coefficient

Subscripts

0	Total quantity
$1, 2$	Cascade inlet / outlet
is	Isentropic
m	Metal angle

Acronyms

AVDR	Axial velocity density ratio
BL	Boundary layer
CFD	Computational fluid dynamics
EU	European Union
GTF	Geared turbofan
HS, LS	High-speed, low-speed
LE, TE	Leading / trailing edge
LPT	Low-pressure turbine
MS	Cascade midspan
RANS	Reynolds averaged Navier-Stokes
SM	Senior & Miller [40] model
SS, PS	Suction / pressure side

References

[1] J. D. Coull and H. P. Hodson. “Predicting the Profile Loss of High-Lift Low Pressure Turbines”. In: *Journal of Turbomachinery* 134.2 (June 2011), p. 021002.

[2] T. J. Praisner and J. P. Clark. “Predicting Transition in Turbomachinery—Part I: A Review and New Model Development”. In: *Journal of Turbomachinery* 129.1 (Mar. 2004), pp. 1–13.

[3] T. J. Praisner, E. A. Grover, M. J. Rice, and J. P. Clark. “Predicting Transition in Turbomachinery—Part II: Model Validation and Benchmarking”. In: *Journal of Turbomachinery* 129.1 (Mar. 2004), pp. 14–22.

[4] N. Rosafio, G. Lopes, S. Salvadori, S. Lavagnoli, and D. A. Misul. “RANS Prediction of Losses and Transition Onset in a High-Speed Low-Pressure Turbine Cascade”. In: *Energies* 16.21 (2023), p. 7348.

[5] J. Hourmouziadis. “Aerodynamic design of low pressure turbines”. In: *AGARD, Blading Design for Axial Turbomachines 40 p(SEE N 89-27661 22-07)* (1989).

[6] E. M. Curtis, H. P. Hodson, M. R. Banieghbal, J. D. Denton, R. J. Howell, and N. W. Harvey. “Development of Blade Profiles for Low-Pressure Turbine Applications”. In: *Journal of Turbomachinery* 119.3 (July 1997), pp. 531–538.

[7] M. Marconcini, F. Rubechini, R. Pacciani, A. Arnone, and F. Bertini. “Redesign of High-Lift Low Pressure Turbine Airfoils for Low Speed Testing”. In: *Journal of Turbomachinery* 134.5 (May 2012), p. 051017.

[8] G. Lopes, L. Simonassi, S. Gendebien, A. F. M. Torre, M. Patinios, N. Zeller, L. Pintat, and S. Lavagnoli. “An Open Test Case for High-Speed Low-Pressure Turbines: The SPLEEN C1 Cascade”. In: *International Journal of Turbomachinery, Propulsion and Power* 10.1 (2025).

[9] S. Lavagnoli, G. Lopes, L. Simonassi, and A. F. M. Torre. *SPLEEN - High Speed Turbine Cascade – Test Case Database*. Version v5. Zenodo, Sept. 2024. DOI: `10.5281/zenodo.13712768`.

[10] G. F. Do Carmo Lopes. “Aerodynamics of a High-Speed Low-Pressure Turbine Cascade with Unsteady Wakes and Purge Flow”. PhD thesis. VKI - von Karman Institute for Fluid Dynamics, Brussels, Belgium, 2024.

[11] A. Halby, B. O. Cakir, L. Da Valle, G. Lopes, M. Okada, and S. Lavagnoli. “On the Application of Background Oriented Schlieren to a Transonic Low-Reynolds Turbine Cascade”. In: *Journal of Turbomachinery* 147.5 (2025).

[12] C. H. Sieverding, M. Stanislas, and J. Snoeck. “The Base Pressure Problem in Transonic Turbine Cascades”. In: *Journal of Engineering for Power* 102.3 (July 1980), pp. 711–718.

[13] A. Melzer and G. Pullan. “The role of vortex shedding in the trailing edge loss of transonic turbine blades”. In: *Journal of Turbomachinery* 141.4 (2019), p. 041001.

[14] R. E. Mayle. “The 1991 IGTI Scholar Lecture: The Role of Laminar-Turbulent Transition in Gas Turbine Engines”. In: *Journal of Turbomachinery* 113.4 (Oct. 1991), pp. 509–536.

[15] E. Dick and S. Kubacki. “Transition Models for Turbomachinery Boundary Layer Flows: A Review”. In: *International Journal of Turbomachinery, Propulsion and Power* 2.2 (2017).

[16] P. Jonáš, O. Mazur, and V. Uruba. “On the receptivity of the by-pass transition to the length scale of the outer stream turbulence”. In: *European Journal of Mechanics-B/Fluids* 19.5 (2000), pp. 707–722.

[17] J. H. Fransson and S. Shahinfar. “On the effect of free-stream turbulence on boundary-layer transition”. In: *Journal of Fluid Mechanics* 899 (2020), A23.

[18] R. E. Mayle, K. Dullenkopf, and A. Schulz. “1997 Best Paper Award—Heat Transfer Committee: The Turbulence That Matters”. In: *Journal of Turbomachinery* 120.3 (July 1998), pp. 402–409.

[19] P. Roach. “The generation of nearly isotropic turbulence by means of grids”. In: *International journal of heat and fluid flow* 8.2 (1987), pp. 82–92.

[20] F. Bertelli, M. Okada, S. Lavagnoli, and K. Hillewaert. “An Active Turbulence Grid for Turbomachinery Flow Experiments”. In: *Journal of Turbomachinery* 147.8 (2025).

[21] M. Vera and H. P. Hodson. “Low-Speed vs High-Speed Testing of LP Turbine Blade-Wake Interaction”. In: *In16th Symposium on Measuring Techniques in Transonic and Supersonic Flows in Cascades and Turbomachines*. 2002, pp. 23–24.

[22] A. Hatman and T. Wang. “A Prediction Model for Separated-Flow Transition”. In: *Journal of Turbomachinery* 121.3 (July 1999), pp. 594–602.

[23] M. Giovannini, M. Marconcini, F. Rubechini, A. Arnone, and F. Bertini. “Scaling Three-Dimensional Low-Pressure Turbine Blades for Low-Speed Testing”. In: *Journal of Turbomachinery* 138.11 (2016), p. 111001.

[24] J. Michálek, A. Ilikan, and T. Arts. “A comparison of high and low speed aerodynamic performance of a very high lift low pressure turbine airfoil (T108) at low Reynolds numbers: Experimental analysis and numerical prediction”. In: *9th European Conference on Turbomachinery: Fluid Dynamics and Thermodynamics, ETC 2011 - Conference Proceedings* 2 (Jan. 2011), pp. 1121–1135.

[25] R. Houtermans, T. Coton, and T. Arts. “Aerodynamic Performance of a Very High Lift Low Pressure Turbine Blade With Emphasis on Separation Prediction ”. In: *Journal of Turbomachinery* 126.3 (Sept. 2004), pp. 406–413.

[26] J. D. Coull and H. P. Hodson. “Blade loading and its application in the mean-line design of low pressure turbines”. In: *Journal of Turbomachinery* 135.2 (2013), p. 021032.

[27] J. D. Coull. "Endwall Loss in Turbine Cascades". In: *Journal of Turbomachinery* 139.8 (Mar. 2017), p. 081004.

[28] M. Drela and H. Youngren. "A User's Guide to MISES 2.53". In: *Massachusetts Institute of Technology, Cambridge, MA* (1998).

[29] H. H. Youngren. "Analysis and design of transonic cascades with splitter vanes". PhD thesis. Massachusetts Institute of Technology, 1991.

[30] B. Abu-Ghannam and R. Shaw. "Natural transition of boundary layers—the effects of turbulence, pressure gradient, and flow history". In: *Journal of Mechanical Engineering Science* 22.5 (1980), pp. 213–228.

[31] M. Drela. "MISES implementation of modified Abu-Ghannam/Shaw transition criterion". In: *Mises User's Guide, MIT* (1995).

[32] G. Lopes, L. Simonassi, A. Torre, M. Patinios, and S. Lavagnoli. "An experimental test case for transonic low-pressure turbines-part 2: Cascade aerodynamics at on-and off-design reynolds and mach numbers". In: *Turbo Expo: Power for Land, Sea, and Air*. Vol. 86106. American Society of Mechanical Engineers. 2022, V10BT30A027.

[33] B. M. Kulfan. "Universal parametric geometry representation method". In: *Journal of aircraft* 45.1 (2008), pp. 142–158.

[34] C. J. Clark. "A Step Towards an Intelligent Aerodynamic Design Process". In: *Turbo Expo: Power for Land, Sea, and Air*. Vol. 58578. American Society of Mechanical Engineers. 2019, V02CT41A033.

[35] J. D. Coull. "Wake induced transition in low pressure turbines". PhD thesis. University of Cambridge, 2010.

[36] R. B. Langtry and F. R. Menter. "Correlation-based transition modeling for unstructured parallelized computational fluid dynamics codes". In: *AIAA journal* 47.12 (2009), pp. 2894–2906.

[37] L. E. Brown. "Axial Flow Compressor and Turbine Loss Coefficients: A Comparison of Several Parameters". In: *Journal of Engineering for Power* 94.3 (July 1972), pp. 193–201.

[38] D. Cadrecha and R. Vazquez. "Profile loss model for low-pressure turbines". In: *9th European Conference on Turbomachinery, Fluid Dynamics and Thermodynamics, Istambul, Turkey*. 2011, pp. 21–25.

[39] J. D. Denton. *Loss mechanisms in turbomachines*. Vol. 78897. American Society of Mechanical Engineers, 1993.

[40] A. C. Senior and R. J. Miller. "A data-centric approach to loss mechanisms". In: *Journal of Turbomachinery* 146.4 (2024).